CRYSTAL GROWTH & DESIGN

pubs.acs.org/crystal

Article

Structural and Electrical Characterizations of BiSb Topological Insulator Layers Epitaxially Integrated on GaAs

Dima Sadek, Richard Daubriac, Corentin Durand, Richard Monflier, Quentin Gravelier, Arnaud Proietti, Fuccio Cristiano, Alexandre Arnoult, and Sébastien R. Plissard*

Cite This: https://doi.org/10.1021/acs.cgd.2c00585

Read Online

ACCESS | Metrics & More | Article Recommendations | Supporting Information

ABSTRACT: Topological insulators (TIs) are known as promising materials for new nanoelectronics and spintronics applications thanks to their unique physical properties. Among these TIs, bismuth antimony alloys ($Bi_{1-x}Sb_x$) remain the most interesting because their electronic band structure can be controlled by changing the stoichiometry, the thickness, or the temperature. However, integrating these materials on an industrial substrate remains a challenge. Here, we investigate the growth, structural, and electrical properties of BiSb materials epitaxially deposited on industrial GaAs(001) substrates. We report the influence of key growth parameters such as temperature, antimony composition, thickness, and growth rate on the crystal quality. We manage to optimize the growth conditions while keeping the $Bi_{1-x}Sb_x$ composition within the TI range. Despite the large lattice mismatch and different crystalline matrices between the deposited material and the substrate, we successfully grow high-quality BiSb(0001) films. For optimized growth conditions, n-type semiconductor behavior of the BiSb layer is demonstrated at temperatures above 100 K. The material band gap calculated from our transport measurements corresponds to that mentioned in the literature. A change of the carrier type from bulk electrons to surface holes is observed when decreasing the temperature below 55 K. Hole mobilities up to 7620 $cm^2/(V{\cdot}s)$ are extracted. This is, to our knowledge, the first demonstration of TI integrated on an industrial substrate keeping its protected surface states.

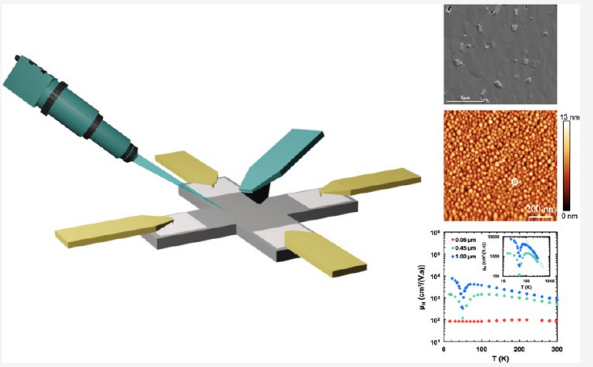

1. INTRODUCTION

Topological insulators (TIs) are a new class of materials that were developed over the last 15 years and have great potential for quantum computers and spintronics applications.[1,2] This new phase of matter is characterized by an inverted bulk band gap driven by strong spin−orbit interactions. As a direct consequence, the TI surface exhibits metallic states topologically protected from the environment[3] thanks to the combination of time-reversal symmetry and spin−orbit interactions.[4,5] Contrary to hybrid semiconductor−superconductor devices,[6−9] a TI coupled to a superconductor[10] shows promises for harboring and protecting Majorana bound states[11] against environment, thus building extremely robust quantum bits (Qubits).[12] Moreover, considering that some TIs have a large spin Hall angle and a high electrical conductivity,[13] their coupling to a ferromagnetic material[14,15] induces an efficient spin-transfer torque (STT).[13,14] This is considered as the qualitative leap in the realization of magneto-resistive random access memories (MRAM).[13]

Since 2007, numerous TIs have been discovered starting with HgTe for two-dimensional (2D) TIs,[16] bismuth antimony ($Bi_{1-x}Sb_x$) alloys for three-dimensional (3D) TIs,[17] and chalcogenide compounds such as Bi_2Se_3, Sb_2Te_3, and Bi_2Te_3.[18] Nevertheless, $Bi_{1-x}Sb_x$ remains the most interesting one thanks to its high conductivity ($\sim 10^5\ \Omega^{-1}{\cdot}m^{-1}$)[13] and its colossal spin Hall angle (~52).[19] Furthermore, $Bi_{1-x}Sb_x$ is the first 3D TI experimentally confirmed by Hsieh et al.[3] after being theoretically predicted by Fu and Kane.[20] In this latter paper, the authors perform angle-resolved photoemission spectroscopy (ARPES) measurements on a $Bi_{0.9}Sb_{0.1}$ surface and observe metallic surface states crossing the Fermi level an odd number of times along a path connecting two time-reversal-invariant momenta in the same Brillouin zone, a negative Z_2 (−1) topological invariant, and large spin−orbit interactions. Moreover, they study the evolution of the band structure as a function of the alloy composition and report a TI behavior for an antimony composition ranging from 7 to 22%.

Recent studies have shown that two-dimensional (2D) $Bi_{1-x}Sb_x$ layers are of particular interest due to the possibility

Received: May 23, 2022
Revised: June 29, 2022

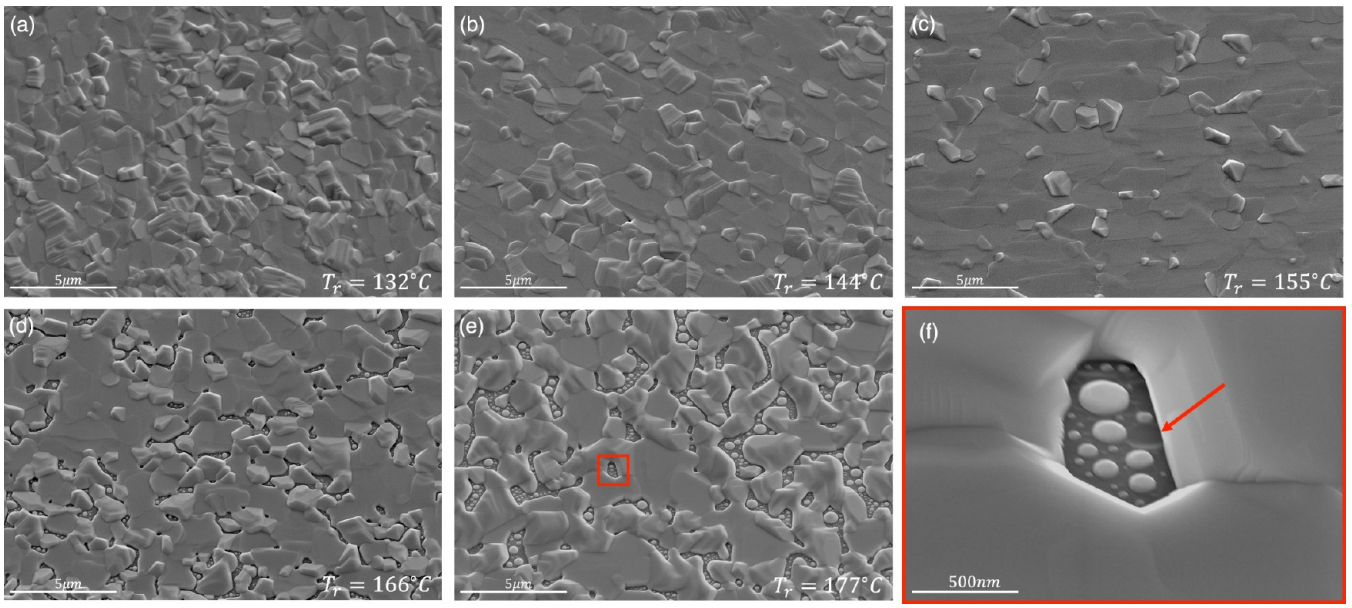

Figure 1. Secondary electron (SE) SEM images showing the surface morphology of the as-grown $Bi_{0.9}Sb_{0.1}$ layer at a growth temperature T_r of (a) 132 °C, (b) 144 °C, (c) 155 °C, (d) 166 °C, and (e) 177 °C. The SEM image in panel (f) is a zoomed image of the area indicated by the red square in panel (e), where adatoms are re-evaporated.

to control their electronic band structure by changing the film thickness, film composition, and the growth direction.[21] It is thus possible to define a variety of Dirac cones at the surface of a $Bi_{1-x}Sb_x$ thin film.[2] Despite numerous studies reporting the growth of BiSb materials,[11,15,22,23] the integration of high-quality thin films on industrial substrates remains challenging due to large lattice mismatches, different crystalline matrices, and difficult surface preparations. Here, our objective is to integrate $Bi_{1-x}Sb_x$ alloys on an industrial GaAs(001) substrate for nanoelectronics and optoelectronics applications. The BiSb crystalline structure is rhombohedral (R-3m), while that of GaAs(001) is cubic and the lattice mismatch between both is 13.7%. To our knowledge, only three papers report the synthesis of a BiSb layer on GaAs(001), including our previous study.[24] In the first one,[13] BiSb(012) layers are obtained on GaAs(001) after deposition of a 3 nm thick MnGa layer (a ferromagnetic layer) but no information is revealed on the sample quality. In the second study,[22] the authors try to grow BiSb directly on GaAs(001) and obtain a textured BiSb thin film.

Here, we investigate the direct integration of high-quality BiSb layers on industrially available GaAs(001) substrates using an MBE412 RIBER molecular beam epitaxy (MBE) system. We study the effect of the growth conditions such as temperature, stoichiometry, film thickness, and growth rate on the structural quality of the BiSb layer. Finally, we demonstrate the excellent electronic properties of such TI materials directly integrated into GaAs(001).

2. METHOD

$Bi_{1-x}Sb_x$ thin films are grown on 2 inch undoped GaAs(001) wafers from AXT in our MBE system. Once the wafers are loaded into the MBE cluster system and the ultrahigh vacuum (UHV) is reached, they are transferred into the preparation chamber for degassing at 300 °C for 1 h. They are then loaded in the growth chamber, which is equipped with a 20 kV STAIB reflection high energy electron diffraction (RHEED) set up. Prior to growth, atomic fluxes (atomic beam equivalent pressures) are calibrated using a Bayard-Alpert gauge. For all of the samples, Ga and As fluxes are chosen to obtain a V/III ratio of 2, and the Sb and Bi fluxes are adapted for each sample. The substrate temperature is probed by both a thermocouple and a band edge measurement (BandiT from kSA). In the following, only "real" temperatures (T_r) measured by BandiT are reported. The correspondence between BandiT temperatures and the thermocouple ones is given in Figure S1. The substrate temperature (T_r) is gradually increased from 100 to 635 °C under an As flux of 1.2×10^{-5} Torr for temperatures above 400 °C. The wafer is deoxidized at 635 °C for 10 min and then the temperature is cooled to 580 °C to grow a 1 μm thick GaAs buffer layer with a V/III ratio of 2 in 1 h. Next, the temperature is cooled to the BiSb growth temperature by keeping the same arsenic flux on 1.2×10^{-5} Torr for the temperature above 400 °C. According to RHEED records, the change in temperature leads to the GaAs(001) surface reconstruction transitioning from $\beta_2(2 \times 4)$ to $c(4 \times 4)$ when the temperature is below 505 °C.[25] Finally, after temperature stabilization, the BiSb growth is initiated (terminated) by opening (closing) simultaneously the Bi and Sb shutters. The BiSb thickness and composition are determined by X-ray diffraction (XRD) in a Bruker D8-Discover diffractometer, and the surface morphology is characterized by scanning electron microscopy (SEM, FEI Aztec-600i) and atomic force microscopy (AFM). Further electron backscattering diffraction (EBSD) measurements are carried out in a FEG-SEM JEOL JSM 7100F equipped with a Nordlys Nano EBSD camera (Oxford Instruments) to obtain an EBSD map and EBSD pole figures of the samples. XRD pole figures are obtained using the Bruker D8-Discover diffractometer. Finally, Hall measurements are performed to investigate the electronic properties of BiSb films.

3. RESULTS AND DISCUSSION

3.1. Influence of Temperature. The initial growths are performed to find the optimum temperature window to grow $Bi_{1-x}Sb_x$ films on GaAs(001) substrates with x being in the TI

https://doi.org/10.1021/acs.cgd.2c00585
Cryst. Growth Des. XXXX, XXX, XXX−XXX

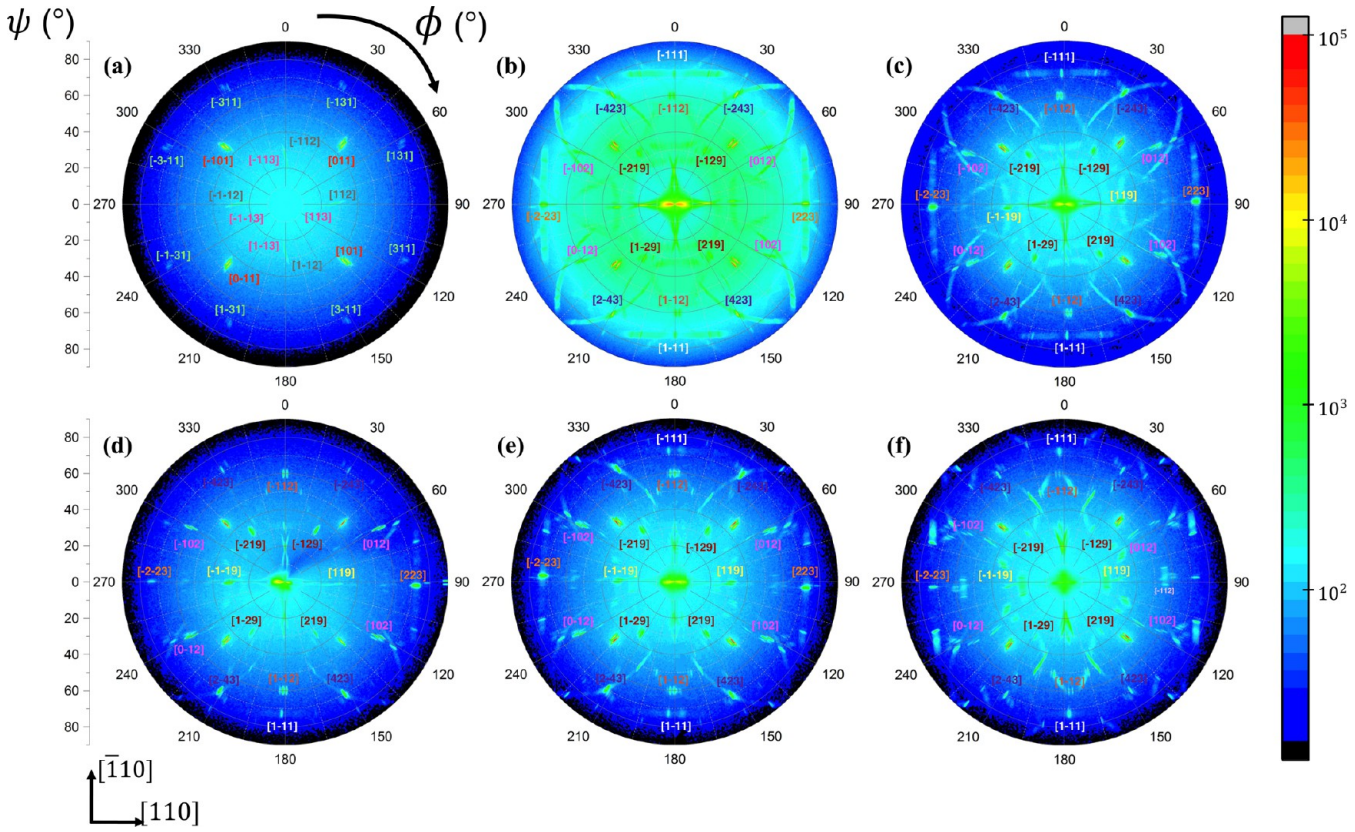

Figure 2. XRD pole figures of different samples using a θ–2θ configuration around the diffraction Bragg angles of the BiSb {0006} planes. (a) A reference measure on the GaAs(001) substrate is provided. The XRD pole figures of the BiSb thin films are reported (b) for the growth temperature of 132 °C, (c) for 144 °C, (d) for 155 °C, (e) for 166 °C, and (f) for 177 °C. The color scale on the right corresponds to the X-ray diffracted intensity of the samples in a logarithmic scale. Labels near each spot correspond to the (hkl) planes. All pole figures are performed by rotating the sample around its normal axis (ϕ) at an angular orientation (ψ) of the sample, ranging from 0 to 90°.

range. Five 250 nm thick layers are thus grown with an antimony composition of 10% and growth temperatures (T_r) of 132, 144, 155, 166, and 177 °C (thermocouple temperatures of 180, 200, 220, 240, and 260 °C, respectively). The Bi and Sb fluxes are 4.5×10^{-7} and 5×10^{-8} Torr, respectively. Scanning electron microscopy (SEM) images of these samples are presented in Figure 1. It shows that the growth is polycrystalline and that the surface morphology is directly dependent on the temperature. For T_r = 132 °C (Figure 1a), the surface is rough and has a large number of misoriented grains. Increasing the temperature (Figure 1b,c) decreases the surface roughness, increases the grain size, and optimizes their orientations: more grains present a flat top facet for T_r = 155 °C. However, increasing the temperature further (Figure 1d,e) worsens the situation: the density of misoriented grains increases and holes appear in the BiSb film. This can be explained by evaporation of bismuth adatoms from the substrate surface due to its low saturation vapor pressure. Figure 1f clearly shows the effect of high temperature (T_r = 177 °C): the red arrow highlights a BiSb droplet that was evaporated after being absorbed at the substrate surface. The melting point of the BiSb system under UHV seems to be around T_r = 177 °C, lower than that calculated at the atmospheric pressure (~271 °C, see Supporting Information Figure S2). According to this series, a growth window around 155 °C is favored to achieve a high crystallinity of $Bi_{0.9}$ $Sb_{0.1}$ films.

To investigate the in-plane epitaxial relationship between the BiSb layer and the GaAs(001) substrate and to probe the temperature dependence of the BiSb texture, XRD pole figure measurements were carried out (see Figure 2). For reference, the pole figure of the GaAs(001) substrate taken at the Bragg diffraction angles of BiSb(0006) is presented in Figure 2a. It can be noticed that no peak is present at Ψ = 0° and that {011}, {112}, {113}, and {311} diffraction peaks are observed with a typical square geometry. Figure 2b–f presents the stereographic projection of BiSb films. All of these figures are obtained at $\theta \sim 23°$ corresponding to the (0006) planes of the BiSb layers. The x-axis corresponds to the [110] direction and y-axis to the [$\bar{1}$10] one. First, in Figure 2b–f, the central peak, corresponding to Ψ = 0°, has a strong intensity, which demonstrates a preferential [0001] growth direction of the BiSb layer. Moreover, all diffraction spots detected in the reference pole figure are also observed at the same position in Figure 2b–f giving evidence that BiSb(0001) does not present any rotation with respect to the GaAs(001) substrate: $[11\bar{2}0]_{BiSb} = [110]_{GaAs}$. This is in good agreement with the theoretical model reported in Supporting Information Figure S3 and our previous study.[24] Interestingly, the central peak is elongated along the [110] direction for all $Bi_{0.9}Sb_{0.1}$ samples (Figure 2b–e) except the one grown at T_r = 177 °C (Figure 2f). This indicates a [110] anisotropic tilt direction for temperatures below 166 °C. For $Bi_{0.9}Sb_{0.1}$ films grown at T_r = 132 °C, the intensity is distributed over the entire pole figure (Figure 2b), indicating that the grain orientations are randomly distributed. On the contrary, increasing the temperature to 144 °C leads to a focus of peak intensities at specific Ψ angles and

https://doi.org/10.1021/acs.cgd.2c00585
Cryst. Growth Des. XXXX, XXX, XXX–XXX

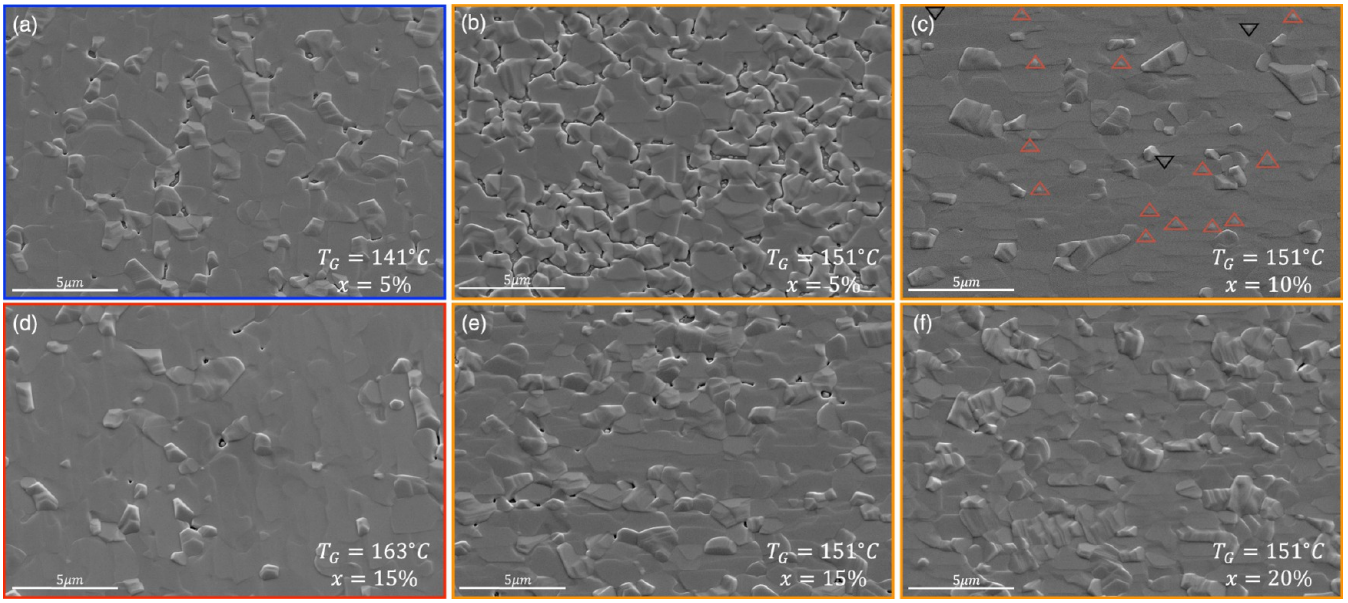

Figure 3. Evolution of the BiSb surface morphology as a function of the temperature (T_r) and the Sb composition (x). SEM images of the BiSb layer grown on a GaAs(001) substrate with different compositions (a, b) 5%; (d, e) 15%; (c) 10%; and (f) 20%. The blue, orange, and red frames indicate growth temperatures of 141, 151, and 163 °C, respectively.

the appearance of axiotaxial rings.[26] This indicates that the surface is starting to organize but still presents an axiotaxial texture and misoriented grains. No more rings are visible, and spots are more intense at T_r = 155 °C, which highlights a good crystalline arrangement and surface organization. Finally, axiotaxial rings appear again for temperatures above 166 °C, indicating an increase of the misoriented grain density in different directions. For T_r = 177 °C, the partial disappearance of the central peak shows the loss of the (0001) preferential growth orientation.

3.2. Influence of the Composition. After fine-tuning the growth temperature to T_r = 151 °C to reduce the surface roughness, we worked on the antimony composition of the BiSb layer. Four 250 nm thick samples were grown by keeping a Bi flux of 4.5 × 10^{-7} Torr and adapting the Sb one for compositions of 5, 10, 15, and 20%. Interestingly, the final composition of the BiSb layer, measured by XRD, corresponds roughly to the beam equivalent pressure (BEP) ratio of each element. Consequently, Sb fluxes of 2.26 × 10^{-8}, 5.00 × 10^{-8}, 7.94 × 10^{-8}, and 11.25 × 10^{-8} Torr are used for composition of 5, 10,15, and 20%, respectively.

The surface morphology of the $Bi_{0.95}Sb_{0.05}$, $Bi_{0.9}Sb_{0.1}$, $Bi_{0.85}Sb_{0.15}$ and $Bi_{0.8}Sb_{0.2}$ samples is shown in Figure 3b,c,e,f, respectively. It can be noticed that in the case of a low Sb composition (5%), the surface is rougher, disorganized, and has a large number of holes compared to other samples. On the opposite, when the Sb composition is 10%, the surface morphology becomes organized due to the nucleation of a great number of grains having a flat top facet. It can be noticed additionally that some grains have a triangular shape pointing upward (see the red triangles) or downward (see the black triangles) in the $[\bar{1}10]$ direction. This indicates a good epitaxial relationship between BiSb films and the GaAs(001) substrate. Finally, increasing further the Sb composition (15 and 20%) leads to an increase in the misoriented grain density and to the appearance of holes, which affect the BiSb film quality. This trend proves the necessity to adapt the growth temperature to the Sb composition. Feutelais et al.[27] have shown that the phase diagram of bismuth−antimony alloys exhibits a continuous solid solution phase (Supporting Information Figure S2), which is strongly affected by the Sb composition. More antimony yields to an increase of the melting point and therefore changes the optimal growth temperature.

To assess the relationship between the composition (x) and the growth temperature (T_r), $Bi_{0.95}Sb_{0.05}$ and $Bi_{0.85}Sb_{0.15}$ samples were grown at 141 and 163 °C, respectively (Figure 3a,d). Interestingly, the surface morphology of these samples is totally different from those grown at 151 °C for the same Sb compositions: they are smoother and better organized. The BiSb alloy quality therefore strongly depends on the x and T_r combination: $Bi_{0.95}Sb_{0.05}$ is optimized around 141 °C, $Bi_{0.9}Sb_{0.1}$ at 151 °C, and $Bi_{0.85}Sb_{0.15}$ has a better surface morphology at 163 °C. Consequently, increasing the composition must be accompanied by an increase of the growth temperature to achieve high crystallinity.

In our previous article,[24] electron backscattering diffraction (EBSD) measurements were carried out on the four samples grown at T_r = 151 °C and confirmed the high crystallinity of the $Bi_{0.9}Sb_{0.1}$ film since it has more than 80% of grains having a negligible tilt (lower than 5°) with respect to the substrate (Supporting Information Figure S4a−d). Moreover, Sb composition dependence of the grain orientation is directly detected; increasing antimony promotes a grain tilting around 10°, while it is between 20 and 35° for low antimony compositions (Supporting Information Figure S4e). Interestingly, there is a link between the grain size and their orientation: the more negligible their tilt, the larger they are (Supporting Information Figure S4f). Indeed, grains having a flat top facet overgrow laterally until they develop enough and coalesce. On the other hand, some misoriented grains keep developing while others disappear and merge with flat top-faced grains. The BiSb nucleation mechanism will be further discussed in the following section.

To probe the influence of the Sb composition on the grain tilting direction, pole figures obtained from EBSD measurements were analyzed on these samples. Figure 4 shows the

https://doi.org/10.1021/acs.cgd.2c00585
Cryst. Growth Des. XXXX, XXX, XXX−XXX

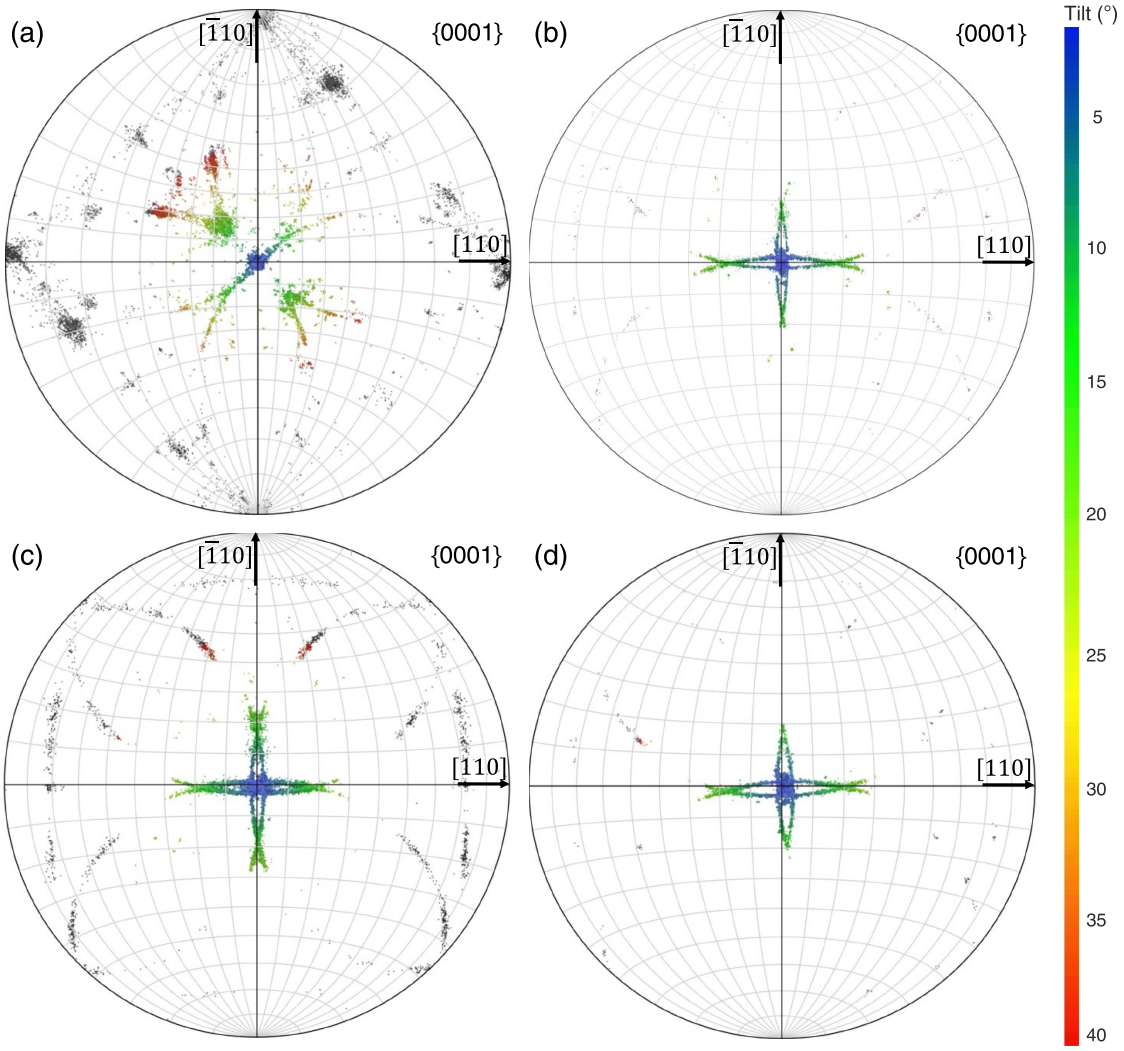

Figure 4. EBSD pole figures of the {0001} planes for different BiSb compositions: (a) $Bi_{0.95}Sb_{0.05}$, (b) $Bi_{0.9}Sb_{0.1}$, (c) $Bi_{0.85}Sb_{0.15}$, and (d) $Bi_{0.8}Sb_{0.2}$. The *x*-axis corresponds to the GaAs [110] direction, whereas it is [−110] for the *y*-axis. The color scale on the right presents the tilt angle ranging from 0 to 40°.

{0001} EBSD pole figures, where the x-axis corresponds to the [110] direction and the y-axis to the [$\bar{1}$10] one. It can be noted that the grain tilting directions depend on the Sb composition. For an Sb composition of 5% (Figure 4a), the grains having a tilt lower than 40° present two preferential tilt direction, the [100] or [010] ones. Moreover, gray spots of unknown orientation are observed and form a 45° tilt square. On the contrary, for an Sb composition greater than 5%, the grain tilt direction is distributed uniformly in either the [110] or the [$\bar{1}$10] direction (Figure 4b–d). These results reveal that more antimony (≥10%) improves the grain nucleation mechanism, which promotes uniformity in grain tilt distribution. They also make it possible to deduce that reducing the Sb composition to 5% with T_r = 151 °C leads to a rotation of the BiSb layer of 45° with respect to the GaAs(001) substrate $[10\bar{1}0]_{Bi_{0.95}Sb_{0.05}} = [110]_{GaAs}$. Finally, to define grain orientation indexed in gray, {10$\bar{1}$0}, {11$\bar{2}$0}, {1$\bar{1}$02}, and {1$\bar{1}$0$\bar{1}$} pole figures were taken for the four samples (Supporting Information Figures S5–S8). Regardless of the composition, no specific grain orientation is observed.

3.3. Influence of the Thickness. To further investigate the growth mode, a thickness series was synthesized. Six samples of different thicknesses ranging from 2 to 450 nm are grown under the same conditions. The $Bi_{0.9}Sb_{0.1}$ growth is initiated by opening both Bi and Sb shutters at the same time with a flow of 4.5×10^{-7} and 5×10^{-8} Torr, respectively. The growth temperature is fixed at 151 °C, and the growth is terminated once the sample thickness is established. After growth, AFM, SEM, and Hall measurements are carried out on these samples.

Figure 5a–f shows AFM images of different $Bi_{0.9}Sb_{0.1}$ thin films having a thickness of 2, 20, 30, 60, 90, and 450 nm, respectively. At the early stage of growth (2 nm), different islands can be observed at the substrate surface (Figure 5a), which indicates a Volmer–Weber growth mode. These islands will expand over time and merge with neighbor ones to form bigger grains as observed for the 20 nm thick layer (Figure 5b). Once a critical density is achieved, for sample thicknesses above 30 nm, the grains develop, become larger, and coalesce, leading to the formation of a continuous layer (Figure 5c–f). To define a critical thickness, corresponding to the grain coalescence, an in situ optical monitoring of the wafer curvature was carried out on the 90 nm thick sample.[28] This measurement records the accumulated stress during the BiSb growth (see Figure S9). At the beginning of the BiSb growth, a

https://doi.org/10.1021/acs.cgd.2c00585
Cryst. Growth Des. XXXX, XXX, XXX–XXX

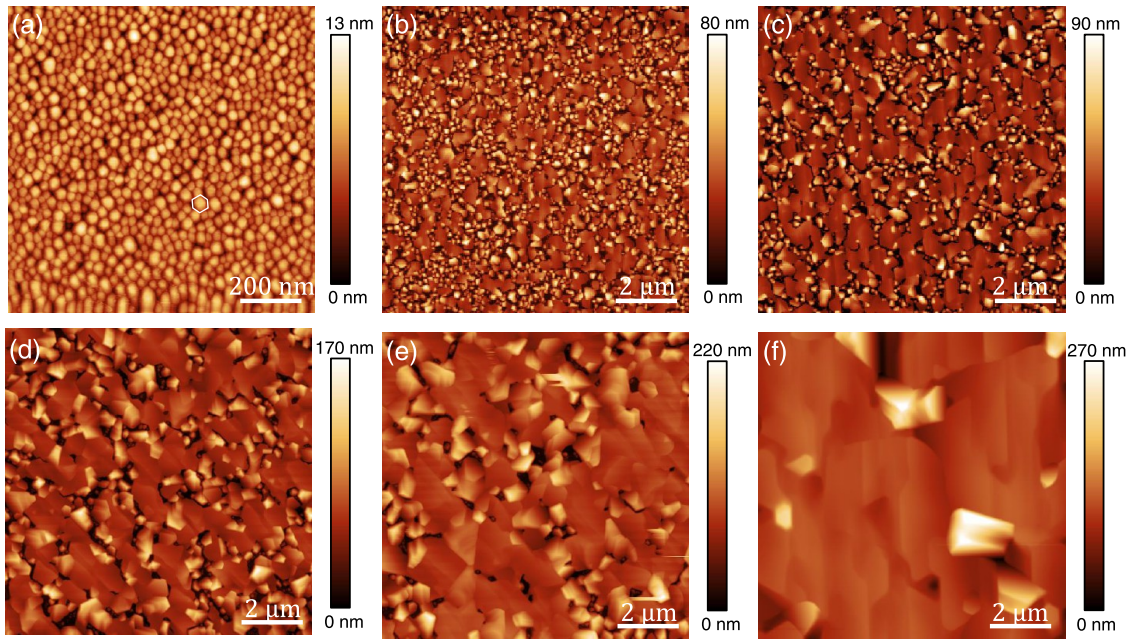

Figure 5. Evolution of the surface morphology as a function of the BiSb layer thickness. The AFM images are taken for thicknessess of (a) 2 nm, (b) 20 nm, (c) 30 nm, (d) 60 nm, (e) 90 nm, and (f) 450 nm. Note that holes are present in the BiSb layer for thicknesses below 450 nm.

compressive stress appears on the wafer corresponding to the grain nucleation. After a ∼12 nm growth, the compressive strain changes into a tensile one, which corresponds to the coalescence of small islands as confirmed in Figure S10a,b. Finally, after 30 nm, the accumulated stress reaches a plateau when the interconnected grains start forming a continuous network, slowly transforming into a continuous layer (Figure 5c−f). Importantly, the larger the thickness, the larger the grains with a flat upper facet. Initially, for a thickness of 2 nm, the grains seem to have almost the same size and have a homogenous arrangement on the substrate (see Figures 5a and S10a). However, this distribution becomes a little less homogenous by increasing the sample thickness to 10−20 nm (see Figures 5b and S10b,c), where some grains develop and others disappear. These results indicate that the larger the grains, the more stable they are since they minimize their surface energy. As a result, the adatoms on the substrate surface and even the small grains tend to migrate and merge with the larger grains, causing them to grow laterally and some existing small ones to disappear.

Starting from 30 nm, corresponding to Figures 5c and S10d, adatoms accumulate around the flat-topped grains, which lead to their lateral overgrowth and finally to their coalescence with neighbors leading to the creation of a continuous layer. These results confirm that our $Bi_{1-x}Sb_x$ growths are controlled by thermodynamics rather than kinetics: it is favorable for adatoms to stick to an existing island compared to nucleate a new one. Small islands are desorbed and absorbed by bigger ones. To favor this mechanism and grow large and flat grains, the kinetics of the system should be slowed down to promote thermodynamics (see the following section). Moreover, it is worth mentioning that the hexagonal shape grains are observed in Figure 5a, confirming the (0001) growth direction from nucleation.

3.4. Influence of the Kinetics on the Growth. To probe further the growth mechanisms of the BiSb layer, four samples with an Sb composition of 10% were synthesized with different growth rates and a total layer thickness of 200 nm. Once the sample temperature is stabilized at 151 °C, the Bi and Sb shutters are opened simultaneously for different growth rates of 0.064, 0.129, 0.26, and 0.385 μm/h and closed simultaneously after 200, 100, 50, and 30 min, respectively. At this growth temperature, the BiSb system is in stable phase according to the BiSb phase diagram,[29] which means that the evaporation rate is almost zero. SEM imaging of these samples is reported in Figure 6.

It can be noticed that a high growth rate favors island growth (Figure 6a), whereas a low growth rate favors two-dimensional (2D) layers growth (Figure 6d). As a result, the surface morphology for a high growth rate is less organized and presents more misoriented grains (Figure 6a) compared to a low growth rate (Figure 6d). This can be explained by thermodynamics and kinetics considerations. Indeed, the adatoms density (n) at a time t and the mean time interval (Δt) between the atoms' arrival at the substrate surface will change with the growth rate. When the growth rate increases, n increases while Δt decreases and reciprocally. A large Δt (low growth rate) indicates a high probability that an adatom will reach its thermodynamics equilibrium and stick to an existing island. As a consequence, low-energy islands, i.e., flat-topped grains in our system, are favored while decreasing the growth kinetics. They will therefore attract a larger number of adatoms if the growth rate decreases so that their lateral size increases. In the extreme case of a very low growth rate (Figure 6d), a continuous layer of flat-topped grains is achieved leading to an optimized surface morphology of the BiSb layer and improved electrical properties.

3.5. BiSb Electronic Properties. Now that the structural and morphological characteristics of the BiSb layers are optimized for integration on an industrial substrate, we focus on their electrical properties. Three $Bi_{0.9}Sb_{0.1}$ samples of 60 nm, 450 nm, and 1 μm thicknesses are grown at 151 °C using Bi and Sb fluxes of 4.5×10^{-7} and 5×10^{-8} Torr, respectively. Samples are then prepared for electrical characterizations using

https://doi.org/10.1021/acs.cgd.2c00585
Cryst. Growth Des. XXXX, XXX, XXX−XXX

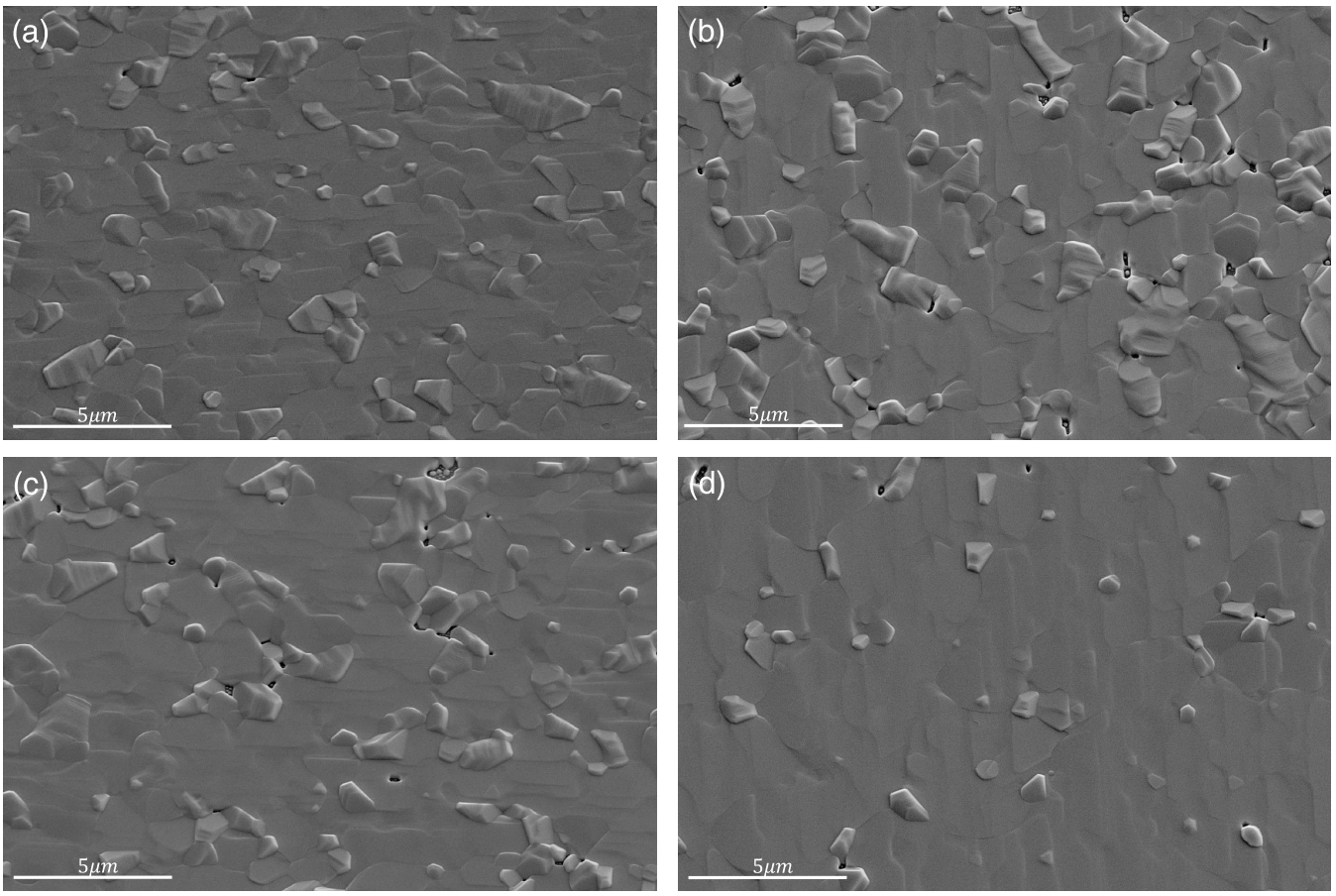

Figure 6. Evolution of the BiSb surface morphology as a function of the growth rate. All layers have the same composition and thickness, and the respective growth rates are (a) 0.385, (b) 0.26, (c) 0.129, and (d) 0.064 μm/h.

the fabrication processes described in the Supporting Information (Figure S11). The electronic properties of BiSb layers were studied following the van der Pauw method. First, the sample sheet resistance R_s is extracted from the standard four-point probe (4PP) measurement. The Hall coefficient R_H is then measured using an external magnetic field of 0.3 Tesla orthogonal to the sample's surface. From these two parameters, we can calculate the Hall sheet concentration N_H and the Hall mobility μ_H.

Figure 7a shows the evolution of the sheet resistance in ohm per square (R_s) as a function of the sample thickness at room temperature. For a 20 nm deposition or below (blue squares in Figure 7a), the samples exhibit a high sheet resistance. As mentioned before, these thicknesses correspond to BiSb materials forming small isolated grains rather than a continuous layer. In these conditions, the current is carried through the GaAs substrate rather than in the BiSb grains, which explains the measured sheet resistance of $R_s \sim 10^7$ Ω/□ close to the substrate one ($\sim 5 \times 10^7$ Ω/□). At 30 nm, the sheet resistance drops quickly since the critical layer thickness is reached. The transition observed in the sheet resistance corresponds to the observed beginning of coalescence of small grains into large interconnected domains (see Figures 5 and S10), opening thus a new channel with a higher conductance. Further increase of the thickness does not increase the size of these domains and leads to a continuous layer (≥90 nm) with much lower sheet resistance, down to 2.3 Ω/□ for a 1 μm thick layer.

Assuming that the current flowing through the GaAs substrate is negligible for thicknesses of 60 nm and beyond, we calculated the resistivities (ρ) from the corresponding sheet resistance values and the BiSb layers' thicknesses. It appears that the resistivity is thickness dependent as shown in Figure 7b. Based on an extended version of the Fuchs−Sondheimer model[30−32] predicting the electrical properties inside polycrystalline thin layers, we extracted an electron mean free path l_g about 265 nm, which is better than the one reported in the literature[33−35] (~150 nm).

In this model, the thin film resistivity is given by

$$\rho_f = \rho_0[1 + \frac{3}{8t}(1 - p)l_0] \quad (1)$$

where ρ_0 and l_0 are, respectively, the bulk crystal resistivity and mean free path, t is the thickness, and p is the probability of carriers being scattered at the surface. In the case of a polycrystalline thin film, Tellier et al.[32] showed that eq 1 remains valid when using ρ_g, the hypothetical polycrystal bulk resistivity, instead of ρ_0 and substituting l_0 by an effective mean free path l_g defined by $l_g \approx \frac{\rho_0}{\rho_g} l_0$. The validity of this model is restricted by grains and boundaries being identical for the different thicknesses and by the t/l_0 ratio being greater than 0.6.[32] In our case, these conditions are verified for layer thicknesses greater than 90 nm (see red diamonds in Figure 7b). In our calculations, we assume that all charge carriers are diffusely scattered at the surface, which means that p, the probability that carriers are specularly reflected at the layer

https://doi.org/10.1021/acs.cgd.2c00585
Cryst. Growth Des. XXXX, XXX, XXX−XXX

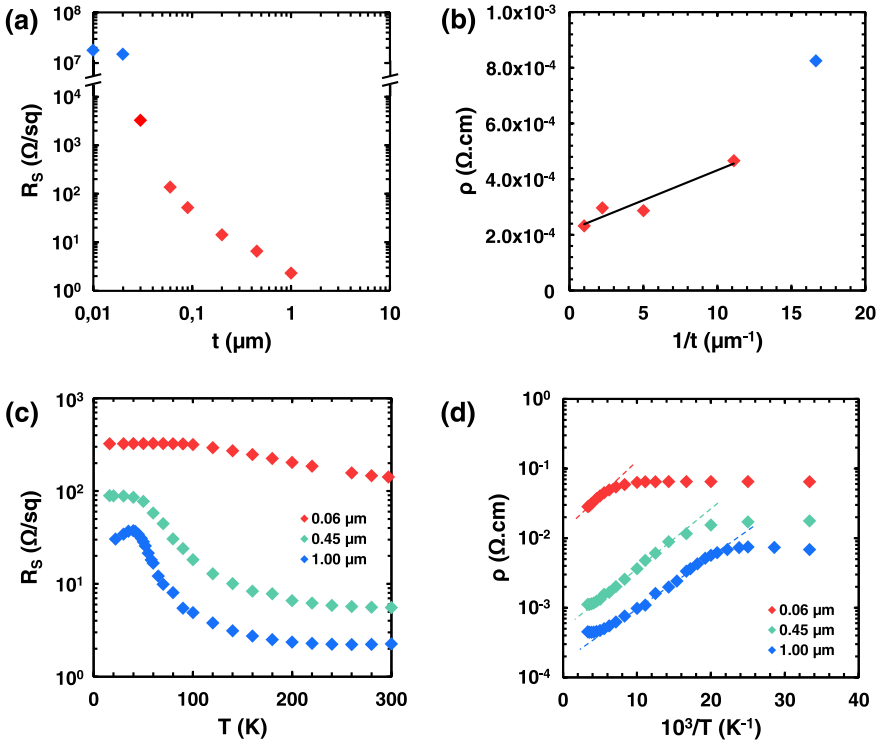

Figure 7. Four-point probe measurements on the BiSb layers. (a) Evolution of the sheet resistance R_s as a function of the BiSb layer thickness t. Blue and red dots refer to nonuniform and continuous grown layers, respectively. (b) Evolution of the resistivity with the inverse thickness. Values depicted in red dots fulfill the Tellier et al.[32] limitation conditions. The electron mean free path is extracted from the slope of the black straight line. (c) Sheet resistance evolution with the temperature for three different BiSb layer thicknesses. (d) Calculated values of the resistivity (from R_s) plotted as a function of the inverse temperature. The activation energies of the BiSb layers can be extracted from the linear dependences at high temperatures, shown in dashed lines.

surface, is considered zero and that the calculated value for l_g is minimized (for p = 0.5, the value of l_g is doubled).

Figure 7c shows the evolution of the sheet resistance R_s as a function of the temperature for the 60 nm, 450 nm, and 1 μm thick samples. For the three thicknesses, the sheet resistance R_s increases as the temperature decreases (starting at T = 300 K), indicating the semiconductor behavior of the BiSb film. The 60 nm curve reaches a plateau for T < 100 K. The 450 nm and 1 μm ones both exhibit a transition around 55 K. Below this temperature, R_s saturates for the 450 nm thick sample and starts decreasing for the 1 μm one. These trends, together with the analysis of the carrier mobility values that will be presented in the following, are consistent with metallic surface states on topological insulators as published in many studies.[36] Figure 7d shows that $\ln(\rho)$ has a linear dependence with $1/T$ for temperatures above the aforementioned transition. This Arrhenius plot of the resistivity ρ indicates a thermally activated behavior. From the slope of the linear fit, we extracted an activation energy for the different thicknesses: 15.4 meV for a 1 μm thick sample, 17.7 meV for the 450 nm one, and 18.0 meV for the 60 nm one. These activation energies are of comparable values to the half of the BiSb band gap energy indicated in the literature,[29] which confirms the nonintentionally doped (NID) semiconductor behavior of our BiSb bulk materials.

The understanding of the electrical properties of the BiSb layers can be pursued by analyzing Hall parameter values. One must consider that only pure Hall values will be analyzed since the Hall scattering coefficient r_H of BiSb is unknown. Figure 8 shows the temperature dependence of (a) the Hall coefficient R_H, (b) the Hall carrier concentration C_H, (c) the absolute value of the Hall sheet carrier concentration N_H below the transition temperature, and (d) the Hall charge carrier mobility μ_H. The first striking feature is that R_H changes the sign from negative to positive at 55 K for the 450 nm and 1 μm thick samples (Figure 8a). At high temperatures, R_H is negative (electrons are the majority carriers), but when decreasing the temperature, it shows an abrupt transition toward positive values (holes are majority carriers). This transition occurs at the same temperature as the one observed in Figure 7c and is consistent with a transition from a bulk to a surface conduction regime (as explained in the following). For the 60 nm thick sample, R_H remains negative over the whole temperature range, exhibiting a different behavior than thicker layers. For all samples and in the high temperature range, carriers are thermally activated, as expected for NID semiconductors, and their concentration decreases while decreasing temperature (Figure 8b). At 300 K, the carrier concentrations per volume of the three samples are in the same order of magnitude ($3-9 \times 10^{19}$ cm^{-3}, Table 1), indicating a similar bulk behavior. On the contrary, below 55 K, the distinction between thick (450 nm and 1 μm) and thin (60 nm) samples is noticeable in Figure 8c. Considering a possible conduction channel at the surface, due to gapless surface states, one cannot consider anymore the carrier concentration per volume at low temperature. Thus, the absolute value of the Hall sheet carrier concentration N_H is reported in Figure 8c. A clear divergence, about one order of magnitude, is visible between thick (450) nm, 1 μm and thin (60 nm) samples. These results are compatible with a BiSb TI behavior at low temperatures and strongly suggest n-type bulk

https://doi.org/10.1021/acs.cgd.2c00585
Cryst. Growth Des. XXXX, XXX, XXX−XXX

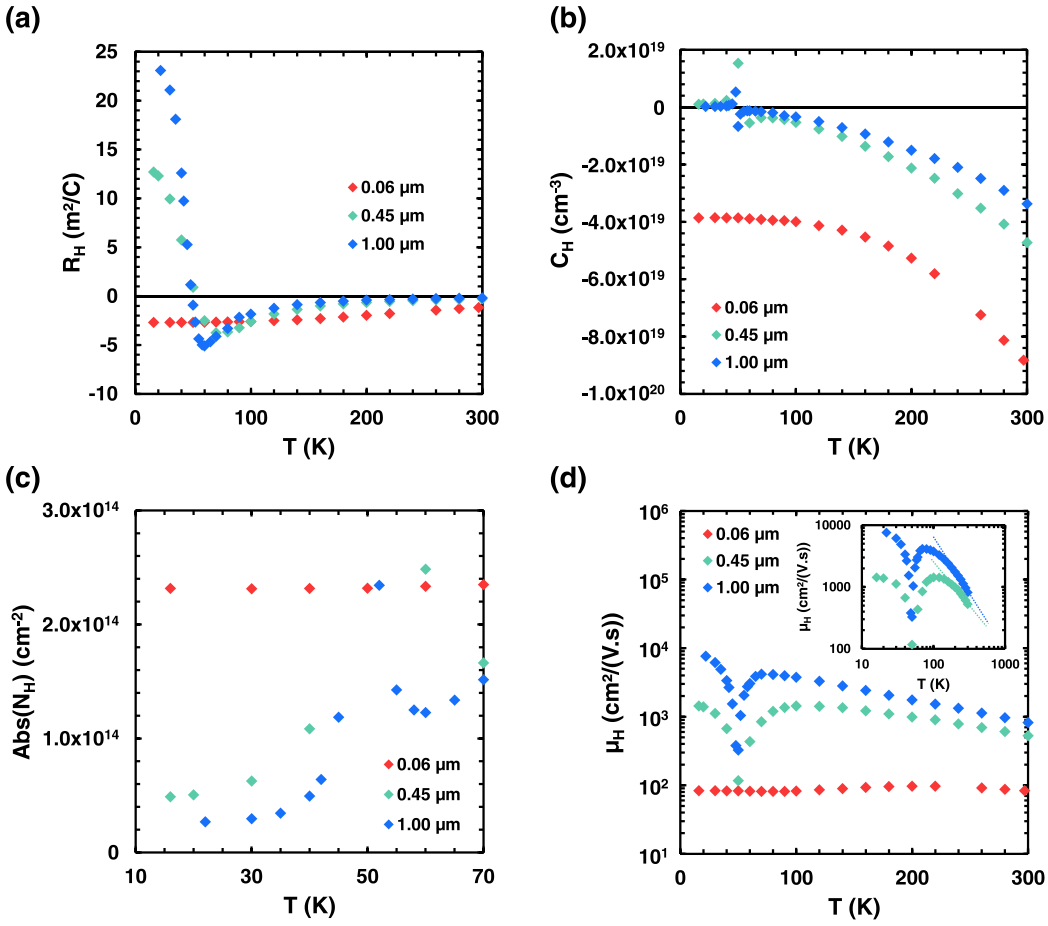

Figure 8. Hall effect measurements on the BiSb layers. (a) Evolution of the Hall coefficient R_H, (b) the Hall concentration C_H, (c) the absolute values of the Hall sheet concentration N_H, and (d) the Hall mobility μ_H as a function of the temperature. The inset in panel (d) shows the Hall mobility as a function of the temperature, in logarithm scales, along with the T^{α} dependencies, in dashed lines.

conduction for all samples at high temperatures (>100 K) and p-type topological surface states for the 450 nm and 1 μm thick samples at low temperatures (<55 K).

Table 1. Hall Concentrations at 300 K and Hall Sheet Concentration at 20 K[a]

thickness (μm)	C_H (300 K) (cm^{-3})	N_H (20 K) (cm^{-2})
0.06	8.82×10^{19} (electrons)	2.32×10^{14} (electrons)
0.45	4.72×10^{19} (electrons)	4.90×10^{13} (holes)
1.00	3.37×10^{19} (electrons)	2.70×10^{13} (holes)

[a]The values are extracted from the Hall effect measurements performed on $Bi_{0,9}Sb_{0.1}$ layers of different thicknesses.

The evolution of the Hall mobilities as a function of the temperature is reported in Figure 8d for the three samples. Here, again, the distinction between thin and thick samples is clearly visible. For the 450 nm and 1 μm samples, the Hall mobilities show a temperature dependence between 100 and 300 K close to $T^{-1.9}$ and $T^{-2.3}$, respectively. These trends are close to those induced by phonon scattering of electrons inside the bulk (known to have $T^{-1.5}$ dependence in conventional semiconductors like silicon[37]). For the thinnest layer, we found a $T^{-0.9}$ dependence between 220 and 300 K. The slope lessening from −2.3 to −0.9 with the thickness reduction might be caused by surface scattering enhancement due to the degraded surface morphology.

At a low temperature (<55 K), the electron Hall mobility of the 60 nm thick sample remains constant around 80 cm^2/(V·s), which is most probably due to its poor morphology and the presence of structural holes in the BiSb layer (see Figure 5). On the contrary, a continuous increase in the hole Hall mobility is reported for the thick samples when decreasing the temperature from 55 to 20 K. The hole mobilities are, respectively, 1430 cm^2/(V·s) at 16 K for the 450 nm thick sample and 7620 cm^2/(V·s) at 22 K for the 1 μm one. Combining the observation of metallic surface states at low temperature (Figure 7c) and the very high hole mobilities (Figure 8d) make it reasonable to assume that these states are topologically protected, which confirms the high quality of our BiSb layers directly integrated into GaAs(0001). This is in good agreement with the BiSb topological insulator phase on (111) surfaces, for which hole-like bands are predicted to have a significant contribution to the surface conduction.[3,19] Finally, it is interesting to note that for temperatures below 55 K, a temperature dependence in $T^{-0.4}$ and $T^{-0.6}$ is observed for the hole mobility (see the inset in Figure 8d). This behavior does not correspond to any known scattering mechanism. Further work is needed to elucidate this point.

4. CONCLUSIONS

In this paper, we have investigated the growth of a $Bi_{1-x}Sb_x$ thin film on an As-rich GaAs(001) cubic substrate using an MBE system. We have shown that despite the large mismatch

https://doi.org/10.1021/acs.cgd.2c00585
Cryst. Growth Des. XXXX, XXX, XXX−XXX

and different crystalline structures between the epitaxial film and the substrate, it is possible to obtain a high-quality BiSb thin film by optimizing the growth conditions. The first crucial step in obtaining an epitaxial BiSb thin film is the substrate surface preparation. Here, the substrate surface was prepared under the As-rich condition with a GaAs growth rate of 1 μm/h and a V/III ratio of 2. Next, we have confirmed the change of the optimal growth temperature as a function of the Sb composition. We report an optimum growth temperature of 151 °C for an Sb composition of 10%, while it is 141 °C for 5% and 163 °C for 15%. These results emphasize the need to increase the temperature with increasing the Sb composition to obtain high crystallinity. By optimizing the growth conditions, it is possible to obtain more than 80% of grains having a negligible tilt with the substrate. Moreover, we report a Volmer−Weber growth mode of the BiSb layer on the GaAs(001) substrate: first, small islands are nucleated on the substrate surface. Grains having a flat-topped facet are favored by decreasing the growth kinetics, and after reaching a critical thickness of ∼30 nm, the islands interconnect and form a continuous layer. Furthermore, the semiconductor behavior of the BiSb layer is demonstrated at temperatures above 100 K. The material band gap calculated from our Hall measurements corresponds to that mentioned in the literature. A change of the carrier type from bulk electrons to surface holes is observed when decreasing the temperature for thicker samples. In that case, high hole mobilities of 1430 and 7620 $cm^2/(V·s)$ are reported for, respectively, 450 nm and 1 μm thick samples at low temperatures. These measurements are in good agreement with the literature and the presence of topologically protected surface states. This is, to our knowledge, the first demonstration of the BiSb topological insulator behavior integrated on an industrial substrate.

■ ASSOCIATED CONTENT

Supporting Information

The Supporting Information is available free of charge at https://pubs.acs.org/doi/10.1021/acs.cgd.2c00585.

Correspondence between thermocouple and BandiT temperatures is provided as well as the theoretical phase diagram of BiSb, the modeling of the pole figure, the EBSD, and the stress measurements and the fabrication processes for Hall devices (PDF)

■ AUTHOR INFORMATION

Corresponding Author

Sébastien R. Plissard − *LAAS-CNRS, Université de Toulouse, CNRS, UPS, F-31400 Toulouse, France;* orcid.org/0000-0002-0769-5429; Email: sebastien.plissard@laas.fr

Authors

Dima Sadek − *LAAS-CNRS, Université de Toulouse, CNRS, UPS, F-31400 Toulouse, France*

Richard Daubriac − *LAAS-CNRS, Université de Toulouse, CNRS, UPS, F-31400 Toulouse, France*

Corentin Durand − *LAAS-CNRS, Université de Toulouse, CNRS, UPS, F-31400 Toulouse, France*

Richard Monflier − *LAAS-CNRS, Université de Toulouse, CNRS, UPS, F-31400 Toulouse, France*

Quentin Gravelier − *LAAS-CNRS, Université de Toulouse, CNRS, UPS, F-31400 Toulouse, France*

Arnaud Proietti − *Centre De Microcaractérisation Raimond Castaing, F-31400 Toulouse, France*

Fuccio Cristiano − *LAAS-CNRS, Université de Toulouse, CNRS, UPS, F-31400 Toulouse, France*

Alexandre Arnoult − *LAAS-CNRS, Université de Toulouse, CNRS, UPS, F-31400 Toulouse, France*

Complete contact information is available at: https://pubs.acs.org/10.1021/acs.cgd.2c00585

Author Contributions

D.S. and S.R.P. conceived the project and experiments. D.S, A.A., and S.R.P grew the samples. D.S. and C.D. performed the AFM measurements and A.P. the EBSD ones. The XRD measurements were carried out by D.S. and A.A. R.D. and Q.G. prepared the samples for Hall effect measurements and carried out the experiments with D.S. R.M., and C.D. D.S., R.D. C.D. F.C. A.A., and S.R.P. analyzed the measurements and wrote the manuscript with input from all of the authors.

Funding

This work was funded by the Agence National de la Recherche (ANR) under grant number ANR-17-PIRE-0001 (HYBRID project).

Notes

The authors declare no competing financial interest.

■ ACKNOWLEDGMENTS

This study benefited from the support of the LAAS-CNRS micro and nanotechnologies platform, member of the French RENATECH network, and was carried out in the EPI-CENTRE common laboratory between Riber and CNRS.

■ REFERENCES

(1) Moore, J. E. The Birth of Topological Insulators. *Nature* **2010**, *464*, 194−198.

(2) Tang, S.; Dresselhaus, M. S. Electronic Properties of Nano-Structured Bismuth-Antimony Materials. *J. Mater. Chem. C* **2014**, *2*, 4710−4726.

(3) Hsieh, D.; Xia, Y.; Wray, L.; Qian, D.; Pal, A.; Dil, J. H.; Osterwalder, J.; Meier, F.; Bihlmayer, G.; Kane, C. L.; Hor, Y. S.; Cava, R. J.; Hasan, M. Z. Observation of Unconventional Quantum Spin Textures in Topological Insulators. *Science* **2009**, *323*, 919−922.

(4) Young, S. M.; Chowdhury, S.; Walter, E. J.; Mele, E. J.; Kane, C. L.; Rappe, A. M. Theoretical Investigation of the Evolution of the Topological Phase of Bi$_2$Se$_3$ under Mechanical Strain. *Phys. Rev. B* **2011**, *84*, No. 085106.

(5) Hasan, M. Z.; Kane, C. L. Colloquium: Topological Insulators. *Rev. Mod. Phys.* **2010**, *82*, 3045−3067.

(6) Hui, H.-Y.; Sau, J. D.; Das Sarma, S. Bulk Disorder in the Superconductor Affects Proximity-Induced Topological Superconductivity. *Phys. Rev. B* **2015**, *92*, No. 174512.

(7) Hui, H.-Y.; Sau, J. D.; Das Sarma, S. Disorder-Induced Subgap States and Majorana Zero-Energy Edge Modes in Two-Dimensional Topological Insulator-Superconductor Hybrid Structures. *Phys. Rev. B* **2014**, *90*, No. 174206.

(8) Chen, J.; Woods, B. D.; Yu, P.; Hocevar, M.; Car, D.; Plissard, S. R.; Bakkers, E. P. A. M.; Stanescu, T. D.; Frolov, S. M. Ubiquitous Non-Majorana Zero-Bias Conductance Peaks in Nanowire Devices. *Phys. Rev. Lett.* **2019**, *123*, No. 107703.

(9) Su, Z.; Zarassi, A.; Hsu, J.-F.; San-Jose, P.; Prada, E.; Aguado, R.; Lee, E. J. H.; Gazibegovic, S.; Op het Veld, R. L. M.; Car, D.; Plissard, S. R.; Hocevar, M.; Pendharkar, M.; Lee, J. S.; Logan, J. A.; Palmstrøm, C. J.; Bakkers, E. P. A. M.; Frolov, S. M. Mirage Andreev Spectra Generated by Mesoscopic Leads in Nanowire Quantum Dots. *Phys. Rev. Lett.* **2018**, *121*, No. 127705.

(10) Yu, W.; Niu, C.-Y.; Zhu, Z.; Cai, X.; Zhang, L.; Bai, S.; Zhao, R.; Jia, Y. Strain Induced Quantum Spin Hall Insulator in Monolayer β-BiSb from First-Principles Study. *RSC Adv.* **2017**, *7*, 27816−27822.
(11) Singh, S.; Romero, A. H. Giant Tunable Rashba Spin Splitting in a Two-Dimensional BiSb Monolayer and in BiSb/AlN Heterostructures. *Phys. Rev. B* **2017**, *95*, No. 165444.
(12) Breunig, O.; Ando, Y. Opportunities in Topological Insulator Devices. *Nat. Rev. Phys.* **2022**, *4*, 184−193.
(13) Khang, N. H. D.; Ueda, Y.; Hai, P. N. A Conductive Topological Insulator with Large Spin Hall Effect for Ultralow Power Spin−Orbit Torque Switching. *Nat. Mater.* **2018**, *17*, 808−813.
(14) Mellnik, A. R.; Lee, J. S.; Richardella, A.; Grab, J. L.; Mintun, P. J.; Fischer, M. H.; Vaezi, A.; Manchon, A.; Kim, E.-A.; Samarth, N.; Ralph, D. C. Spin-Transfer Torque Generated by a Topological Insulator. *Nature* **2014**, *511*, 449−451.
(15) Fan, T.; Khang, N. H. D.; Nakano, S.; Hai, P. N. Ultrahigh Efficient Spin Orbit Torque Magnetization Switching in Fully Sputtered Topological Insulator and Ferromagnet Multilayers. *Sci. Rep.* **2022**, *12*, No. 2998.
(16) Bernevig, B. A.; Hughes, T. L.; Zhang, S.-C. Quantum Spin Hall Effect and Topological Phase Transition in HgTe Quantum Wells. *Science* **2006**, *314*, 1757−1761.
(17) Hsieh, D.; Qian, D.; Wray, L.; Xia, Y.; Hor, Y. S.; Cava, R. J.; Hasan, M. Z. A Topological Dirac Insulator in a Quantum Spin Hall Phase. *Nature* **2008**, *452*, 970−974.
(18) Zhang, H.; Liu, C.-X.; Qi, X.-L.; Dai, X.; Fang, Z.; Zhang, S.-C. Topological Insulators in Bi2Se3, Bi2Te3 and Sb2Te3 with a Single Dirac Cone on the Surface. *Nat. Phys.* **2009**, *5*, 438−442.
(19) Qu, D.-X.; Roberts, S. K.; Chapline, G. F. Observation of Huge Surface Hole Mobility in the Topological Insulator $Bi_{0.91}Sb_{0.09}$ (111). *Phys. Rev. Lett.* **2013**, *111*, No. 176801.
(20) Fu, L.; Kane, C. L. Topological Insulators with Inversion Symmetry. *Phys. Rev. B* **2007**, *76*, No. 045302.
(21) Şahin, C.; Flatté, M. E. Tunable Giant Spin Hall Conductivities in a Strong Spin-Orbit Semimetal: Bi_xSb_{1-x}. *Phys. Rev. Lett.* **2015**, *114*, No. 107201.
(22) Yao, K.; Khang, N. H. D.; Hai, P. N. Influence of Crystal Orientation and Surface Termination on the Growth of BiSb Thin Films on GaAs Substrates. *J. Cryst. Growth* **2019**, *511*, 99−105.
(23) Fan, T.; Tobah, M.; Shirokura, T.; Huynh Duy Khang, N.; Nam Hai, P. Crystal Growth and Characterization of Topological Insulator BiSb Thin Films by Sputtering Deposition on Sapphire Substrates. *Jpn. J. Appl. Phys.* **2020**, *59*, No. 063001.
(24) Sadek, D.; Dhungana, D. S.; Coratger, R.; Durand, C.; Proietti, A.; Gravelier, Q.; Reig, B.; Daran, E.; Fazzini, P. F.; Cristiano, F.; Arnoult, A.; Plissard, S. R. Integration of the Rhombohedral BiSb(0001) Topological Insulator on a Cubic GaAs(001) Substrate. *ACS Appl. Mater. Interfaces* **2021**, *13*, 36492−36498.
(25) LaBella, V. P.; Krause, M. R.; Ding, Z.; Thibado, P. M. Arsenic-Rich GaAs(0 0 1) Surface Structure. *Surf. Sci. Rep.* **2005**, *60*, 1−53.
(26) Detavernier, C.; Özcan, A. S.; Jordan-Sweet, J.; Stach, E. A.; Tersoff, J.; Ross, F. M.; Lavoie, C. An Off-Normal Fibre-like Texture in Thin Films on Single-Crystal Substrates. *Nature* **2003**, *426*, 641−645.
(27) Feutelais, Y.; Morgant, G.; Didry, J. R.; Schnitter, J. Thermodynamic Evaluation of the System Bismuth-Antimony. *Calphad* **1992**, *16*, 111−119.
(28) Arnoult, A.; Colin, J. Magnification Inferred Curvature for Real-Time Curvature Monitoring. *Sci. Rep.* **2021**, *11*, No. 9393.
(29) Lenoir, B.; Dauscher, A.; Cassart, M.; Ravich, YuI.; Scherrer, H. Effect of Antimony Content on the Thermoelectric Figure of Merit of $Bi_{1-x}Sb_x$ Alloys. *J. Phys. Chem. Solids* **1998**, *59*, 129−134.
(30) Fuchs, K. The Conductivity of Thin Metallic Films According to the Electron Theory of Metals. *Math. Proc. Cambridge Philos. Soc.* **1938**, *34*, 100−108.
(31) Mayadas, A. F.; Shatzkes, M. Electrical-Resistivity Model for Polycrystalline Films: The Case of Arbitrary Reflection at External Surfaces. *Phys. Rev. B* **1970**, *1*, 1382−1389.
(32) Tellier, C. R.; Tosser, A. J.; Boutrit, C. The Mayadas-Shatzkes Conduction Model Treated as a Fuchs-Sondheimer Model. *Thin Solid Films* **1977**, *44*, 201−208.
(33) Osmic, E.; Barzola-Quiquia, J.; Böhlmann, W.; Bercoff, P. G.; Venosta, L.; Häussler, P. Thermopower and Magnetotransport Properties of Bi100−xSbx Topological Insulator Thin Films Prepared by Flash Evaporation. *J. Phys. Chem. Solids* **2022**, *167*, No. 110734.
(34) Taskin, A. A.; Segawa, K.; Ando, Y. Oscillatory Angular Dependence of the Magnetoresistance in a Topological Insulator ${\text{Bi}}_{1\ensuremath{-}x}{\text{Sb}}_{x}$. *Phys. Rev. B* **2010**, *82*, No. 121302.
(35) Taskin, A. A.; Ando, Y. Quantum Oscillations in a Topological Insulator ${\text{Bi}}_{1\ensuremath{-}x}{\text{Sb}}_{x}$. *Phys. Rev. B* **2009**, *80*, No. 085303.
(36) Xu, Y.; Miotkowski, I.; Liu, C.; Tian, J.; Nam, H.; Alidoust, N.; Hu, J.; Shih, C.-K.; Hasan, M. Z.; Chen, Y. P. Observation of Topological Surface State Quantum Hall Effect in an Intrinsic Three-Dimensional Topological Insulator. *Nat. Phys.* **2014**, *10*, 956−963.
(37) Stillman, G. E.; Wolfe, C. M. Electrical Characterization of Epitaxial Layers. *Thin Solid Films* **1976**, *31*, 69−88.

https://doi.org/10.1021/acs.cgd.2c00585
Cryst. Growth Des. XXXX, XXX, XXX−XXX